

# P13.2 MULTIPLE-DOPPLER RADAR OBSERVATIONS OF THE STRUCTURE AND EVOLUTION OF VORTICES IN A CONVECTIVE BOUNDARY LAYER

PAUL MARKOWSKI\* AND CHRISTINA HANNON

*Department of Meteorology, Pennsylvania State University, University Park, PA*

## 1. Introduction and motivation

The ubiquity of vortices in convective boundary layers is apparent in many observations and simulations (e.g., Carroll and Ryan 1970, Maxworthy 1973, Cortese and Balachandar 1993, MacPherson and Betts 1997, Schneider and Lilly 1999, Kanak et al. 2000). For example, dust devils are common on sunny days, at least when land surface characteristics allow such vortices to be manifest visually (e.g., Kaimal and Businger 1970, Hess and Spillane 1990, Snow and McClelland 1990). Radar observations of the boundary layer also commonly reveal vortices, probably having a spatial scale larger than dust devils (e.g., Wilson et al. 1992). Some boundary layer vortices have been observed to be associated with cloud development (e.g., Atkins et al. 1995, 1998). These latter observations have led some to hypothesize that boundary layer vortices are an important aspect of convection initiation (e.g., Kingsmill 1995).

Theoretical studies have investigated the formation of vertical vortices within corridors of horizontal wind shear that arise from the instability of shear flows and vortex sheets (e.g., Miles and Howard 1964; Kundu 1990, pp. 391–395). Such processes have been hypothesized to be responsible for the development of boundary layer vertical vortices in some observational studies (e.g., Kingsmill 1995). In other cases, vorticity stretching (e.g., Wilson et al. 1992) and tilting of horizontal vorticity (e.g., Atkins et al. 1995) have been observed to be the dominant contributors to vertical vorticity amplification. Large-eddy simulations of convective boundary layers also have examined the formation of vortices. For example, Kanak et al. (2000) found that local vertical vortices tended to arise within vertical velocity maxima. In their simulations, as well as in idealized, inviscid simulations of isolated buoyant elements by Shapiro and Kanak (2002), no mean wind was prescribed. Kanak et al. (2000) conjectured and Shapiro and Kanak (2002) deduced that horizontal vorticity initially was generated by the density gradients associated with the thermals, and this horizontal vorticity subsequently was tilted by horizontal vertical velocity gradients to yield vertical vorticity.

The dynamics, origin, and evolution of boundary layer vortices could have large relevance to convection initi-

ation owing to the feedbacks between vertical velocity and vorticity. These feedbacks have been studied fairly extensively in theoretical and numerical modeling studies of deep, moist convection (Klemp 1987), but the possibility of similar interactions in boundary layer updrafts, and their ramifications for convection initiation, remain largely unexplored. Prior observational studies of boundary layer vortices have been somewhat limited by their spatial and temporal resolution, which is considerably coarser than what has been available in large-eddy simulations.<sup>1</sup> It is this fact that motivates the present paper.

The purpose of this paper is to use high-resolution (90-s in time, 100 m in space), three-dimensional wind syntheses derived from Doppler radar data to document the finescale structure and evolution of boundary layer vertical vorticity extrema, in addition to the dynamical processes playing a role in the amplification of the vorticity extrema. The radar data were obtained on 12 June 2002 in northwestern Oklahoma during the International H<sub>2</sub>O Project (IHOP). A more descriptive overview of the dataset and analysis techniques is provided in section 2. The most significant observations are presented in sections 3–5. Section 6 contains conclusions and some final remarks.

## 2. Overview and methods

During the afternoon of 12 June 2002, four mobile radars were dispatched to northwestern Oklahoma in anticipation of convection initiation in the proximity of the intersection of an outflow boundary and a dryline. Shallow cumulus clouds were observed within the data analysis region for the first 90 minutes of the deployment. Some towering cumulus clouds developed along the outflow boundary during the 2100–2130 UTC time period, and at the same time, along the dryline to the east, cumulonimbus clouds were initiated.

Radar data were collected continuously from 1936–2130 UTC. Three of the mobile radars [two Doppler On Wheels (DOW) radars and the XPOL radar] were similar to those described by Wurman et al. (1997). The wavelength, stationary half-power beamwidth, range gate spacing, and Nyquist velocity were 3 cm, 0.95°, 75 m, and 16.0 m s<sup>-1</sup>, respectively. The fourth mobile

---

\*Corresponding author address: Dr. Paul Markowski, Department of Meteorology, Pennsylvania State University, 503 Walker Building, University Park, PA 16802; *e-mail*: pmarkowski@psu.edu.

---

<sup>1</sup>We attempt to avoid the difficult issues associated with defining vortices by restricting our terminology to vorticity extrema, maxima, and minima, hereafter.

radar [Shared Mobile Atmospheric Research and Teaching (SMART) radar] has been described by Biggerstaff and Guynes (2000). The wavelength, stationary half-power beamwidth, range gate spacing, and Nyquist velocity were 5 cm,  $1.5^\circ$ , 67 m, and  $14.6 \text{ m s}^{-1}$ , respectively.

Radial velocity errors caused by low signal-to-noise ratio, second-trip echoes, sidelobes, ground clutter, and velocity aliasing were removed prior to interpolating the data to a Cartesian grid. The grid used for the analyses presented herein is  $20 \times 20 \times 2 \text{ km}^3$ , and has a horizontal and vertical grid spacing of 100 m. Interpolation of the radial velocity data to the grid was accomplished with a Barnes objective analysis (Barnes 1964; Koch et al. 1983) using an isotropic, spherical weight function and smoothing parameter,  $\kappa$ , of  $0.36 \text{ km}^2$ . Advection was removed from the objectively analyzed radial velocity grids. The advection velocity was determined using Matejka’s (2002) technique.

The three-dimensional wind field was synthesized using the overdetermined dual-Doppler approach (e.g., Kessinger et al. 1987) and the anelastic mass continuity equation (integrated upward), rather than a direct triple- or quadruple-Doppler solution. The time resolution of the analyses is 90 s. Dynamic retrievals of the pressure perturbation field also were performed, following the technique outlined by Gal-Chen (1978).

### 3. Evolution of the vertical vorticity field

Although the wind syntheses span the 1936–2130 UTC period, the proceeding analysis and discussion focuses on the 2012–2118 UTC time period. Figure 1 depicts the vertical vorticity and vertical velocity fields at 12 min intervals (i.e., every eighth wind synthesis is displayed) from 2012–2118 UTC. Vertical vorticity maxima are observed both along the outflow boundary (e.g., the vorticity maxima identified with numbers “3” and “6” in Fig. 1) and away from the outflow boundary, both on its warm as well as its cool side (e.g., the vorticity maxima identified with numbers “2” and “5” in Fig. 1). Other vorticity maxima evolve from positions away from the outflow boundary to positions along the outflow boundary (e.g., those identified with numbers “1” and “4” in Fig. 1 between 2012–2036 UTC).

A few long-lived ( $>1 \text{ min}$ ) dust devils were witnessed by the radar operators, but it is not known what dynamical relationship, if any, these had to the vorticity maxima observed in the radar-derived wind syntheses. The location of one such dust devil is indicated in Fig. 1 at 2036 UTC. It is perhaps worth noting that the dust devil was located within a relative maximum in the radar-resolved vertical vorticity field.

The motions of the vorticity extrema are generally similar to the ambient, vertically averaged wind velocity in the vicinity of the vorticity extrema. Many extrema also are observed to propagate laterally with respect to the ambient wind direction for brief periods of time, although there is no systematic preference for cyclonic (anticyclonic) vorticity extrema to propagate to the right (left) of the mean shear vector as Maxworthy (1973) observed in the case of dust devils.

What is perhaps most remarkable about Fig. 1 is the time continuity of the vorticity field. Vorticity extrema (e.g., those numbered 1–6 in Fig. 1) can be tracked continuously for the entire radar deployment. The vorticity extrema weaken and strengthen in time and occasionally merge with one another, but the extrema generally fail to dissipate entirely or become unidentifiable in the wind syntheses. *In other words, the very definition of the genesis and dissipation of a vorticity extremum is ambiguous.* It will be shown in section 5 that the vertical vorticity of individual air parcels entering a vorticity extremum can be traced backward in time to values approaching zero, but this does not contradict the finding that a “genesis time” and “end time” could not be defined for the vorticity extrema.

Close inspection of the vertical vorticity fields also reveals many complex interactions among vertical vorticity maxima and between the vertical vorticity and vertical velocity fields. For example, the weaker vorticity extrema occasionally are observed orbiting stronger vorticity extrema, the so-called “Fujiwhara effect” (Fujiwhara 1931). An example of this evolution is observed in proximity to vorticity maximum number 5 during the 2012–2048 UTC period (Fig. 1). In this same region, notice how the vertical velocity field also is rearranged by the interactions between vorticity extrema. Bluestein et al. (2004) have observed similar interactions between dust devils.

During periods in which vertical vorticity amplified, amplification first occurs near the ground and then builds upward in time. Rapid amplification is preceded by updrafts, i.e., vorticity amplification is a byproduct of updrafts. The amplification of low-level vorticity often leads to a weakening of updrafts—and occasionally induces downdrafts—in a manner very similar to the process attributed to occlusion downdraft formation in supercell thunderstorms (Klemp and Rotunno 1983). An example of this evolution is visible at 2100 UTC at the location of vorticity maximum number 3 (Fig. 1).

### 4. Characteristics of the vertical vorticity extrema

The most prominent vertical vorticity maxima, which tend to be located along the outflow boundary and within the warm sector south of the boundary, attain values of  $10^{-2} \text{ s}^{-1}$  (Fig. 1). The most prominent minima attain values of  $-6 \times 10^{-3} \text{ s}^{-1}$ . These amplitudes are less than those in the large eddy simulations conducted by Kanak et al. (2000), but vorticity values are highly resolution-dependent. The grid spacing in the radar analysis domain is approximately three times the horizontal grid spacing in the Kanak et al. simulations. The angular momentum associated with the strongest vorticity maxima, estimated by averaging the vertical vorticity within the area coinciding with the vorticity extremum, range from  $800\text{--}1300 \text{ m}^2 \text{ s}^{-1}$ , which is slightly larger than estimated by Kanak et al. in their simulations.

The magnitudes of the vorticity extrema generally decrease with height from their largest values near the

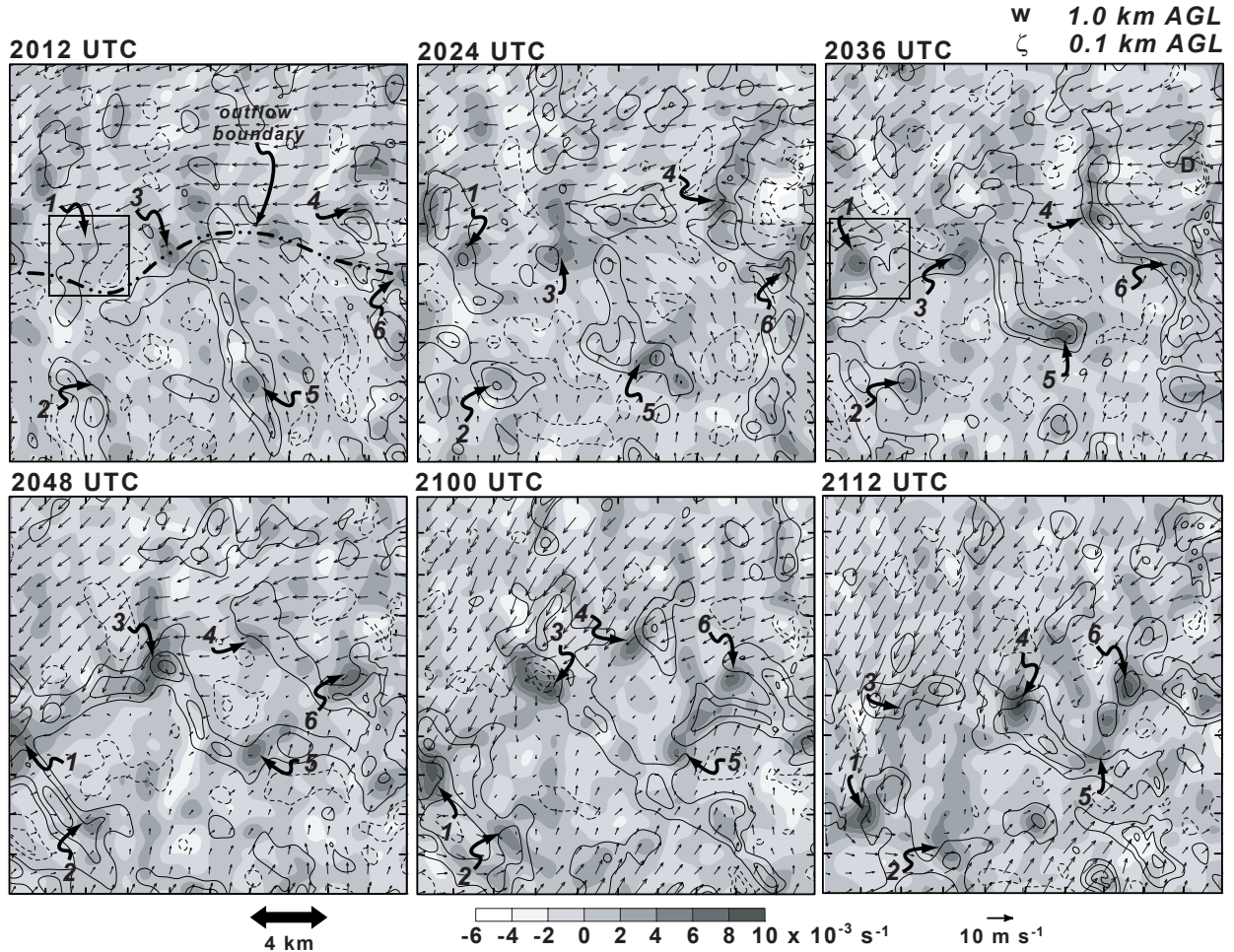


FIG. 1. Horizontal cross sections of vertical vorticity,  $\zeta$ , at 0.1 km (shaded, see scale at bottom), and vertical velocity,  $w$ , at 1.0 km (contoured at  $1 \text{ m s}^{-1}$  intervals, negative contours are dashed, and the  $0 \text{ m s}^{-1}$  contour has been suppressed) at 12-min intervals from 2012–2118 UTC. Horizontal wind vectors also appear on each panel (the tail of each vector is located at every 10th grid point). The position of the outflow boundary is indicated at 2012 UTC. The vorticity maxima discussed in the text are labeled in each panel. The boundaries of the zoomed images displayed in Figs. 2 and 3 are indicated in the 2012 UTC and 2036 UTC panels. The “D” in the northeastern part of the 2036 UTC panel indicates the approximate location of a long-lived, intense dust devil observed visually.

surface, although all of the significant vorticity extrema span the depth of the boundary layer, which is approximately 2 km deep. The vertical vorticity extrema along the outflow boundary also have some tendency to be tilted away from the vertical toward the cool side of the outflow boundary, owing to the enhanced southerly vertical wind shear located along the boundary. The vertical vorticity extrema in the warm sector south of the outflow boundary are nearly vertically stacked as a consequence of the relatively weak vertical wind shear present there.

Retrieved pressure minima are collocated with significant vorticity extrema, presumably a dynamical consequence of the rotation. The amplitudes of these minima are small, with pressure deficits rarely exceeding 0.15 mb compared to the pressure in close proximity to the vorticity extrema. It would not be surprising if the actual pressure fluctuations are considerably larger than those retrieved owing to the smoothing of the pressure field during the retrieval process.

No systematic relationship between the vertical veloc-

ity and vertical vorticity fields is evident, nor can a wavelength between vorticity maxima (e.g., Kingsmill 1995, Richardson et al. 2003) be defined, owing to the highly irregular spatial distribution of vorticity (e.g., Fig. 1). Some vorticity maxima are situated beneath updraft centers, others are located on the flanks of updrafts, and others are located in downdrafts (Fig. 1). It also is curious that circularly symmetric (in a horizontal plane) vorticity maxima occasionally develop beneath quasi-linear updrafts (e.g., vorticity maximum number 5 at 2012 UTC; Fig. 1).

## 5. Vertical vorticity amplification

As shown in section 3, vorticity extrema are observed to persist for the duration of the data collection period. For this reason, and also because the very definition of a vortex is ambiguous, it is difficult to define a time of vortex genesis or demise. Our analyses are limited to the conditions associated with the amplification of *preexist-*

ing vorticity extrema. In this section, we examine the amplification of vorticity maximum number 1. Vorticity maximum number 1 is located along the outflow boundary and undergoes a substantial amplification between 2012 and 2030 UTC, during which time the vertical vorticity increases from  $\sim 0.002 \text{ s}^{-1}$  to  $> 0.007 \text{ s}^{-1}$  (Figs. 2 and 3). The processes associated with the amplification of other vorticity extrema will be described at the conference.

#### a. Contributions to the local vorticity tendency

Neglecting curvature terms and molecular viscosity, the local vertical vorticity change is

$$\begin{aligned} \frac{\partial \zeta}{\partial t} = & \underbrace{-\mathbf{v}_h \cdot \nabla(f + \zeta) - w \frac{\partial \zeta}{\partial z}}_{\text{horizontal and vertical advection}} \underbrace{-(f + \zeta) \nabla \cdot \mathbf{v}_h}_{\text{stretching}} \\ & + \underbrace{\left( \frac{\partial u}{\partial z} \frac{\partial w}{\partial y} - \frac{\partial v}{\partial z} \frac{\partial w}{\partial x} \right)}_{\text{tilting}} + \underbrace{\left( \frac{\partial p}{\partial x} \frac{\partial \alpha}{\partial y} - \frac{\partial p}{\partial y} \frac{\partial \alpha}{\partial x} \right)}_{\text{solenoidal generation}} \\ & + \underbrace{\left( \frac{\partial F_y}{\partial x} - \frac{\partial F_x}{\partial y} \right)}_{\text{turbulent diffusion}} \end{aligned} \quad (1)$$

where  $p$  is pressure,  $\alpha$  is specific volume,  $f$  is the Coriolis parameter, and  $F_x$  and  $F_y$  represent turbulent diffusion of momentum in the  $x$  and  $y$  directions. The solenoidal term is neglected in our analysis. The term is zero if the anelastic approximation is made, and even in the worst case imaginable, with orthogonal isobars and isopycnics in a horizontal plane and with horizontal pressure and temperature gradients of  $1 \text{ mb km}^{-1}$  and  $5 \text{ K km}^{-1}$ , respectively, the term is of order  $2 \times 10^{-6} \text{ s}^{-2}$ . The horizontal pressure and temperature gradients are about an order of magnitude smaller than the above estimates in the case at hand. The diffusion of vorticity also is neglected in our analysis. In the past, a first-order or  $K$ -theory closure based on the Doppler-derived deformation has been applied in order to estimate turbulent diffusion (e.g., Brandes 1984, Hane and Ray 1985), but the effect of vorticity diffusion on the vorticity evolution was found to be much smaller than the other terms (e.g., stretching and tilting; Brandes 1984). Mixing effects may be more significant in the surface layer where airflow deformation and vertical turbulent fluxes are large, but the surface layer is not well-resolved by the radar observations.

At the start of the intensification period (2012 UTC; Fig. 2), vorticity stretching is the largest contributor to the amplification of the vorticity maximum (horizontal advection is a large contributor to the local vertical vorticity tendency, but advection cannot amplify vorticity extrema, only translate or reshape them). At the end of the period of rapid intensification (2030 UTC; Fig. 3), when the vorticity maximum approximately reaches its greatest amplitude, stretching is the largest contributor to vorticity amplification near the ground, and tilting is largest contributor in the middle boundary layer (1.5

km), although mainly on the flanks of the vorticity maximum. Once vertical vorticity begins has intensified near the surface, vertical advection also can become a significant contributor to the local vorticity tendency in the middle boundary layer (not shown; observed for some other vorticity extrema). It is worth noting that the terms producing the largest instantaneous vorticity tendencies do not necessarily contribute in the same proportion to the total integrated vorticity of the air parcels comprising the vorticity maximum, as will be shown in subsection b.

#### b. Contributions to the Lagrangian vorticity tendency

In order to obtain perhaps a more complete understanding of the dynamical processes contributing to the amplification of vorticity maximum number 1, the contributions to the Lagrangian vertical vorticity tendencies are examined for a number of trajectories entering the vorticity maximum. By integrating the Lagrangian form of (1), and neglecting the curvature, solenoidal, and turbulent diffusion terms as before, the vertical vorticity of a parcel,  $\zeta(t)$ , can be written as

$$\begin{aligned} \zeta(t) &= \zeta_o - \int_o^t (f + \zeta) \nabla \cdot \mathbf{v}_h dt' \\ &+ \int_o^t \left( \frac{\partial u}{\partial z} \frac{\partial w}{\partial y} - \frac{\partial v}{\partial z} \frac{\partial w}{\partial x} \right) dt' \\ &= \zeta_o + \zeta_{\text{stretching}} + \zeta_{\text{tilting}}, \end{aligned} \quad (2)$$

where  $\zeta_o$  is the vertical vorticity of the parcel at the start of the integration ( $t = 0$ ) and  $\zeta_{\text{stretching}}$  and  $\zeta_{\text{tilting}}$  are the total contributions to  $\zeta$  from stretching and tilting, respectively. Trajectories are computed using trilinear spatial interpolation and a fourth-order Runge-Kutta time integration algorithm using a time step of 10 s. The three-dimensional wind fields are assumed to vary linearly in time between the two Doppler analyses closest to the current time of a point along a trajectory.

Equation (2) is integrated along four trajectories for vorticity maximum number 1 from 2012–2033 UTC. The four trajectories pass through the maximum vertical vorticity value at 2033 UTC at 0.1, 0.5, 1.0, and 1.5 km (trajectories “A,” “B,” “C,” and “D,” respectively; see Fig. 4). The differences between  $\zeta$  and  $\zeta_o + \zeta_{\text{stretching}} + \zeta_{\text{tilting}}$  are generally less than  $1 \times 10^{-3} \text{ s}^{-1}$ . The relatively small residuals are perhaps indicative of the quality of the velocity data (e.g., its accuracy and space and time resolution) and the relative unimportance of any parameterized subgrid turbulent diffusion (a consequence of the relatively fine spatial resolution). The largest disagreement between  $\zeta$  and  $\zeta_o + \zeta_{\text{stretching}} + \zeta_{\text{tilting}}$  ( $\sim 4 \times 10^{-3} \text{ s}^{-1}$ ) is for the near-ground trajectories entering vorticity maximum number 1 (Fig. 4), and is perhaps due to inadequately resolved velocity gradients in that portion of the domain near the surface.

Along the near-ground trajectories entering vorticity maximum number 1 (trajectories “A” and “B” in Fig. 4),  $\zeta_{\text{stretching}}$  is the dominant contributor to  $\zeta$ , not surprisingly, since tilting goes to zero at the ground. For trajec-

2012 UTC

# Vorticity Maximum #1

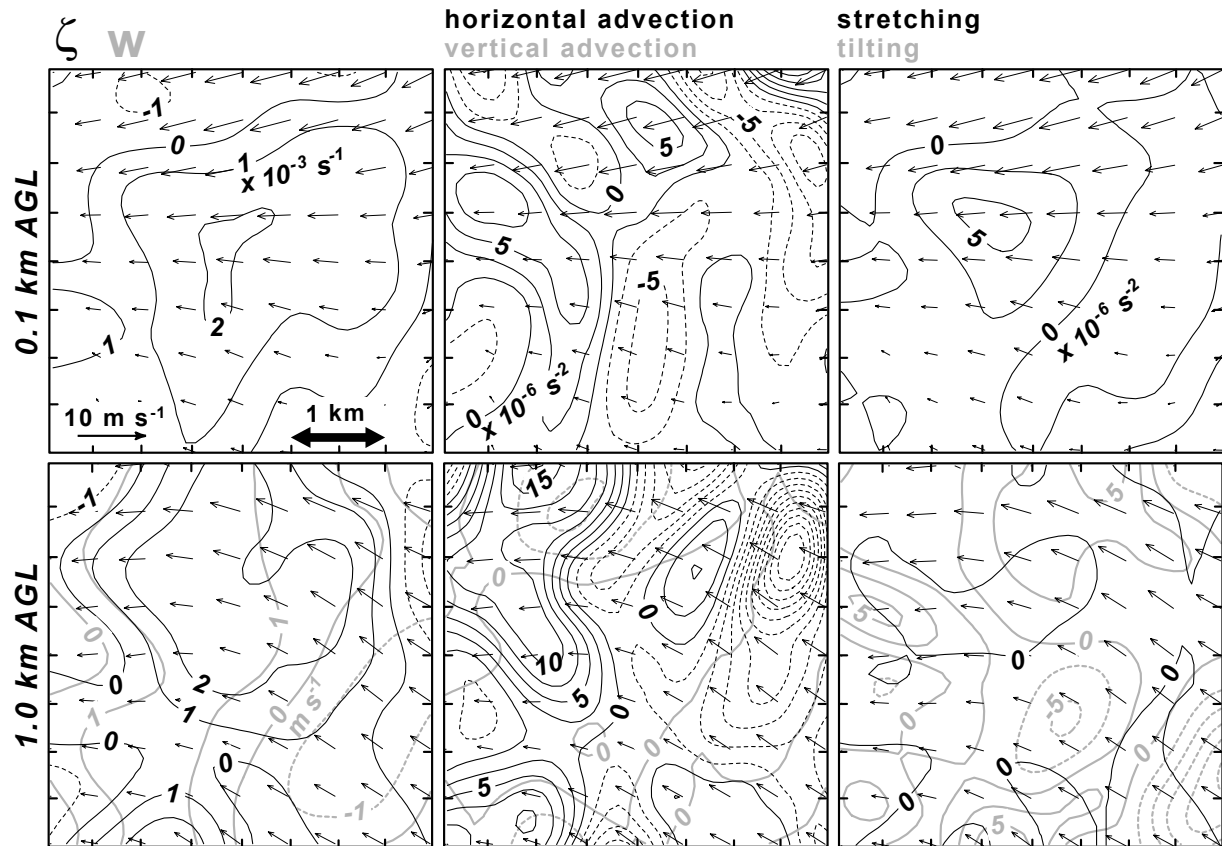


FIG. 2. (Left) Horizontal cross sections of vertical vorticity,  $\zeta$ , and vertical velocity,  $w$ , at 0.1 km (top left) and 1.0 km (bottom left) in the proximity of vorticity maximum number 1 at 2012 UTC (refer to Fig. 1). Vertical vorticity (black) is contoured at  $1 \times 10^{-3} \text{ s}^{-1}$  intervals, with negative contours dashed. Vertical velocity (gray) is contoured at  $1 \text{ m s}^{-1}$  intervals, with negative contours dashed. (Center) Horizontal cross sections of horizontal and vertical advection of vertical vorticity at 0.1 km (top center) and 1.0 km (bottom center). Horizontal advection (black) is contoured at  $2.5 \times 10^{-6} \text{ s}^{-2}$  intervals, with negative contours dashed. Vertical advection (gray) also is contoured at  $2.5 \times 10^{-6} \text{ s}^{-2}$  intervals, with negative contours dashed. (Right) Horizontal cross sections of vorticity stretching and tilting at 0.1 km (top right) and 1.0 km (bottom right). Stretching (black) is contoured at  $2.5 \times 10^{-6} \text{ s}^{-2}$  intervals, with negative contours dashed. Tilting (gray) also is contoured at  $2.5 \times 10^{-6} \text{ s}^{-2}$  intervals, with negative contours dashed.

ories entering vorticity maximum number 1 at 1.0 and 1.5 km (trajectories “C” and “D” in Fig. 4),  $\zeta_{\text{tilting}}$  assumes progressively larger roles, and in fact is the dominant contributor to  $\zeta$  along trajectory “D.” Comparisons of the vorticity budgets for the parcels entering vorticity maximum number 1 to the budgets of parcels entering other vorticity maxima (not shown) indicate that the relative importance of tilting versus stretching varies from one vorticity extremum to another (and seems to be a function of the amount of horizontal vorticity present in the boundary layer). Thus, it is difficult to generalize when it comes to the dynamical processes responsible for the amplification of boundary layer vorticity extrema. Stretching virtually always will dominate near the surface, but above the surface the dominant contributors to vertical vorticity vary from case to case, and even from one vorticity extremum to another.

## 6. Summary and conclusions

This paper has documented the evolution, characteristics, and dynamics of vertical vorticity extrema observed by mobile Doppler radars in a convective boundary layer during the 12 June 2002 IHOP deployment. The observations support the following conclusions:

1. The vertical vorticity field has remarkable time continuity, such that many vorticity extrema could be tracked continuously for the entire deployment spanning nearly 2 hours.
2. The vertical vorticity extrema decrease in amplitude with height and are tilted by the vertical wind shear.
3. Periods of vertical vorticity amplification involve the superpositioning of an updraft; the air parcels comprising the vorticity maxima can acquire their vorticity from stretching or tilting, although the contributions can vary significantly from one vor-

2030 UTC

# Vorticity Maximum #1

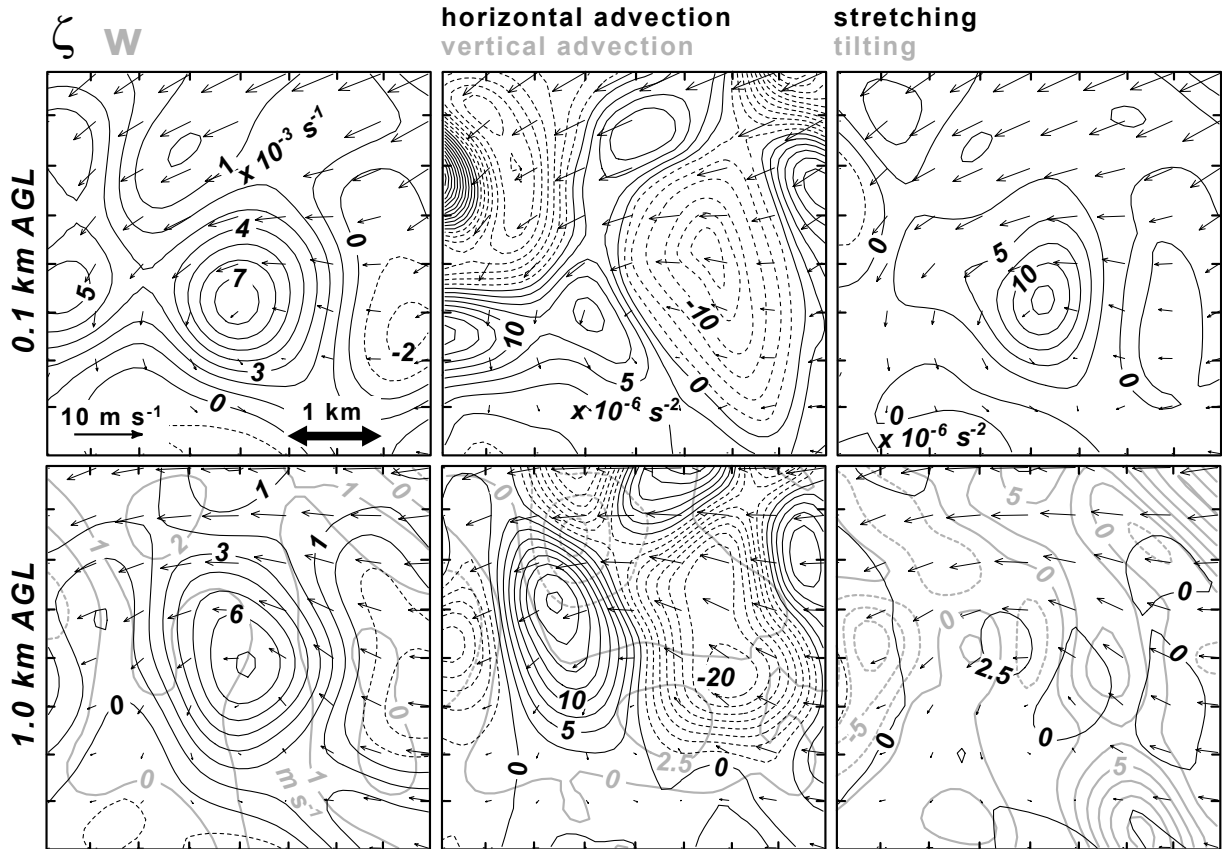


FIG. 3: As in Fig. 2, but for 2030 UTC (refer to Fig. 1).

ticity maximum to another, and from one elevation to another, making it difficult to generalize about the dynamical processes responsible for the amplification of vorticity.

4. The vertical vorticity extrema are associated with pressure minima; given that the vorticity extrema weaken with height, vorticity anomalies tend to be associated with a downward-directed vertical pressure gradient force.
5. The interactions among vorticity maxima and between vertical vorticity maxima and the vertical velocity field are horribly complex; if such interactions are later shown to be crucial to convection initiation, it may be difficult to develop general guidelines for the prediction of convection initiation.

We have avoided one obvious question throughout: *what is the origin of vertical vorticity in the boundary layer?* The sequence of wind syntheses reveals that vorticity anomalies can be tracked for long periods of time (>1 h). Many vorticity anomalies persisted for the entire data collection period, intensifying and weakening depending on the superpositioning of boundary layer drafts, to which the vorticity anomalies unavoidably feed back. Observationally, we cannot find some hypothetical initial time when  $\zeta = 0$  everywhere.

Does surface friction play a role in generating vertical vorticity? How about slow, but nonzero baroclinic generation of vertical vorticity by horizontal solenoids possibly associated with thermals? Or horizontal vorticity generation by solenoids in the vertical plane, which subsequently can be tilted by gradients in the vertical motion field to produce vertical vorticity (e.g., Shapiro and Kanak 2002)? We do not have the data to address the contribution of surface friction to vertical vorticity, and it is questionable whether baroclinic effects could be observed adequately. In situ thermodynamic observations currently cannot sample thermodynamic fields with the level of detail to address baroclinic vorticity generation by thermals, and buoyancy fields retrieved from four-dimensional radar data are unavoidably noisy owing to the fact that they depend on an extra (time) derivative of the velocity fields. Furthermore, there is the issue of how vertical vorticity arises at the surface. Davies-Jones (1982) argued that a downdraft is necessary for tornado formation in environments devoid of preexisting vertical vorticity at the surface. Are downdrafts in the convective boundary layer similarly necessary for vertical vorticity to arise at the surface?

Ongoing work includes investigation of the helicity of the vorticity extrema and corresponding suppression of mixing, two-dimensional shearing instability, and the

## Vorticity Maximum #1

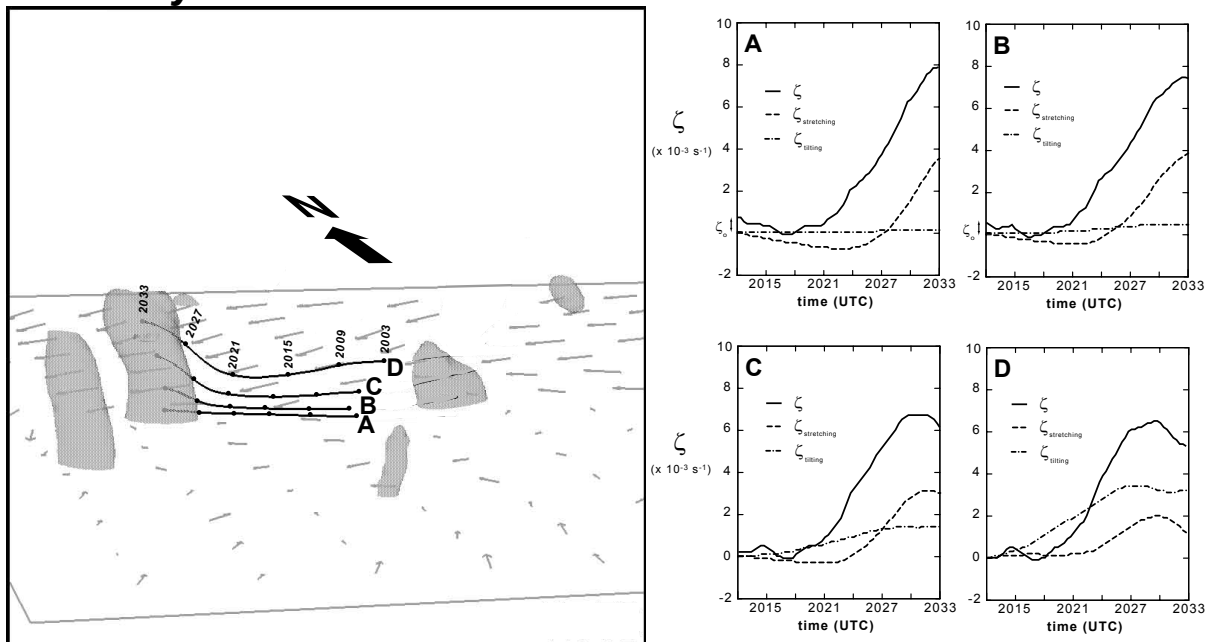


FIG. 4. (Left) Trajectories entering vorticity maximum number 1 between 2003–2033 UTC. The four trajectories shown pass through the location of the maximum vertical vorticity at 0.1 km (trajectory “A”), 0.5 km (trajectory “B”), 1.0 km (trajectory “C”), and 1.5 km (trajectory “D”). Parcel locations at 6-min intervals along each trajectory are indicated (UTC time). The view is from the south. The gray arrows represent the horizontal wind vectors at 0.1 km and the gray surface is the  $5 \times 10^{-3} \text{ s}^{-1}$  vertical vorticity isosurface. (Right) The integrated contributions to the total vertical vorticity,  $\zeta$ , along trajectories A, B, C, and D, as a function of time. Neglecting turbulent diffusion, the total vertical vorticity following a parcel can be expressed as  $\zeta = \zeta_0 + \zeta_{\text{stretching}} + \zeta_{\text{tilting}}$ , where  $\zeta_0$  is the vertical vorticity of the air parcel at the start of the integration,  $\zeta_{\text{stretching}}$  is the contribution from stretching, and  $\zeta_{\text{tilting}}$  is the contribution from tilting.

demise of vorticity extrema. Preliminary analyses of the helicity and eddy viscosity fields indicate that it may be difficult to generalize about the role of rotation in reducing mixing within updrafts. Preliminary analyses also suggest that the demise of many strong vorticity extrema is brought about by the vortex valve effect and an adverse vertical pressure gradient that reverses the sign of vorticity stretching.

*Acknowledgments.* We are grateful for the thought-provoking discussions with Drs. Kathy Kanak, Yvette Richardson, Erik Rasmussen, Josh Wurman, Tammy Weckwerth, and Conrad Ziegler regarding this work. We also acknowledge Dr. Jerry Guynes, Curtis Alexander, and Nettie Arnott for their assistance with the SMART-radar and DOW datasets. Software developed by the National Center for Atmospheric Research was relied upon heavily in this work. Radar editing was performed using SOLO, objective analyses of radar data were produced by REORDER, and wind syntheses were produced by CEDRIC. The Vis5d visualization software created by the Space Science and Engineering Center at the University of Wisconsin was used for one of the figures (Fig. 4) appearing in this paper. This research was supported by National Science Foundation grant ATM-0130307 made to Pennsylvania State University.

### REFERENCES

- Atkins, N. T., R. M. Wakimoto, and T. M. Weckwerth, 1995: Observations of the sea-breeze front during CaPE: Part II: Dual-Doppler and aircraft analysis. *Mon. Wea. Rev.*, **123**, 944–969.
- Atkins, N. T., R. M. Wakimoto, and C. L. Ziegler, 1998: Observations of the finescale structure of a dryline during VORTEX 95. *Mon. Wea. Rev.*, **126**, 525–550.
- Barnes, S. L., 1964: A technique for maximizing details in numerical weather map analysis. *J. Appl. Meteor.*, **3**, 396–409.
- Biggerstaff, M. I., and J. Guynes, 2000: A new tool for atmospheric research. Preprints, *20th Conf. on Severe Local Storms*, Orlando, Amer. Meteor. Soc., 277–280.
- Bluestein, H. B., C. C. Weiss, and A. L. Pazmany, 2004: Doppler radar observations of dust devils in Texas. *Mon. Wea. Rev.*, **132**, 209–224.
- Brandes, E. A., 1984: Vertical vorticity generation and mesocyclone sustenance in tornadic thunderstorms: The observational evidence. *Mon. Wea. Rev.*, **112**, 2253–2269.
- Carroll, J. J., and J. A. Ryan, 1970: Atmospheric vorticity and dust devil rotation. *J. Geophys. Res.*, **75**, 5179–5184.
- Cortese, T., and S. Balachandrar, 1993: Vortical nature of thermal plumes in turbulent convection. *Phys. Fluids*, **A5**, 3226–3232.
- Davies-Jones, R. P., 1982: A new look at the vorticity equation with application to tornadogenesis. Preprints, *Twelfth Conf. on Severe Local Storms*, San Antonio, Amer. Meteor. Soc., 249–252.
- Fujiwhara, S., 1931: Short note on the behavior of two vortices. *Proc. Phys.-Math. Soc. Japan*, **13**, 106–110.
- Gal-Chen, T., 1978: A method for the initialization of the anelastic equations: Implications for matching models with observations. *Mon. Wea. Rev.*, **106**, 587–606.
- Hane, C. E., and P. S. Ray, 1985: Pressure and buoyancy fields derived from Doppler radar data in a tornadic thunderstorm. *J. Atmos. Sci.*, **42**, 18–35.
- Hess, G. D., and K. T. Spillane, 1990: Characteristics of dust devils in Australia. *J. Appl. Meteor.*, **29**, 498–507.
- Kanak, K. M., D. K. Lilly, and J. T. Snow, 2000: The formation of vertical vortices in the convective boundary layer. *Quart. J. Roy. Meteor. Soc.*, **126A**, 2789–2810.
- Kaimal, J. C., and J. A. Businger, 1970: Case studies of a convective plume and a dust devil. *J. Appl. Meteor.*, **9**, 612–620.
- Kessinger, C. J., P. S. Ray, and C. E. Hane, 1987: The Oklahoma squall line of 19 May 1977. Part I: A multiple Doppler analysis of convective and stratiform structure. *J. Atmos. Sci.*, **44**, 2840–2864.
- Kingsmill, D. E., 1995: Convection initiation associated with a sea-breeze front, a gust front, and their collision. *Mon. Wea. Rev.*, **123**, 2913–2933.

- Klemp, J. B., 1987: Dynamics of tornadic thunderstorms. *Ann. Rev. Fluid Mech.*, **19**, 369–402.
- Klemp, J. B., and R. Rotunno, 1983: A study of the tornadic region within a supercell thunderstorm. *J. Atmos. Sci.*, **40**, 359–377.
- Koch, S. E., M. DesJardins, and P. J. Kocin, 1983: An interactive Barnes objective map analysis scheme for use with satellite and conventional data. *J. Clim. Appl. Meteor.*, **22**, 1487–1503.
- Lugt, H. J., 1979: The dilemma of defining a vortex. *Recent Developments in Theoretical and Experimental Fluid Mechanics*, U. Muller, K. G. Roesner, and B. Schmidt, Eds., Springer-Verlag, 309–321.
- MacPherson, J. I., and A. K. Betts, 1997: Aircraft encounters with strong coherent vortices over the boreal forest. *J. Geophys. Res.*, **102**, D24, 29231–29234.
- Matejka, T., 2002: Estimating the most steady frame of reference from Doppler radar data. *J. Atmos. Oceanic Tech.*, **19**, 1035–1048.
- Maxworthy, T., 1973: A vorticity source for large scale dust devils and other comments on naturally occurring columnar vortices. *J. Atmos. Sci.*, **30**, 1717–1722.
- Richardon, Y. P., J. M. Wurman, and C. Hartman, 2003: Multi-Doppler analysis of convective initiation on 19 June 2002 during IHOP. Preprints, *31st International Conf. on Radar Meteorology*. Seattle, Amer. Meteor. Soc., 793–795.
- Schaefer, J. T., 1986: The dryline. *Mesoscale Meteorology and Forecasting*, P. S. Ray, Ed., Amer. Meteor. Soc., 549–572.
- Schneider, J. M., and D. K. Lilly, 1999: An observational and numerical study of a sheared, convective boundary layer. Part I: Phoenix II observations, statistical description, and visualization. *J. Atmos. Sci.*, **56**, 3059–3078.
- Segal, M., J. F. W. Purdom, J. L. Song, R. A. Pielke, and Y. Mahrer, 1986: Evaluation of cloud shading effects on the generation and modification of mesoscale circulations. *Mon. Wea. Rev.*, **114**, 1201–1212.
- Segal, M., and R. W. Arritt, 1992: Nonclassical mesoscale circulations caused by surface sensible heat-flux gradients. *Bull. Amer. Meteor. Soc.*, **73**, 1593–1604.
- Shapiro, A., and K. M. Kanak, 2002: Vortex formation in ellipsoidal thermal bubbles. *J. Atmos. Sci.*, **59**, 2253–2269.
- Snow, J. T., and T. M. McClelland, 1990: Dust devils at White Sands Missile Range, New Mexico. Part I: Temporal and spatial distribution. *J. Geophys. Res.*, **95**, 13707–13721.
- Wilson, J. W., G. B. Foote, N. A. Crook, J. C. Fankhauser, C. G. Wade, J. D. Tuttle, and C. K. Mueller, 1992: The role of boundary-layer convergence zones and horizontal rolls in the initiation of thunderstorms: A case study. *Mon. Wea. Rev.*, **120**, 1785–1815.
- Wurman, J. M., J. M. Straka, E. N. Rasmussen, M. Randall, and A. Zahrai, 1997: Design and deployment of a portable, pencil-beam, pulsed, 3-cm Doppler radar. *J. Atmos. Oceanic Technol.*, **14**, 1502–1512.